POLITECNICO MILANO 1863

DIPARTIMENTO DI MECCANICA

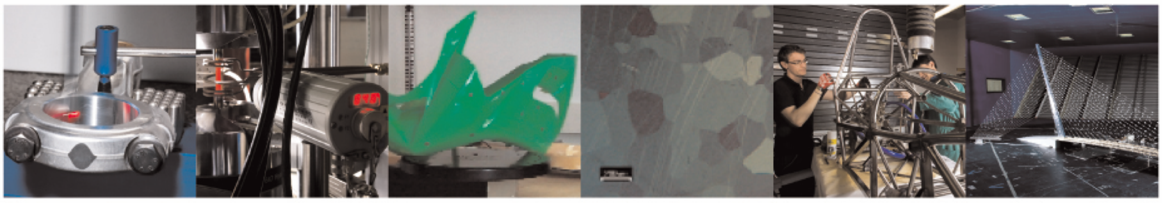

A multibody non-linear model of the post-derailment dynamics of a railway vehicle

Matteo Santelia, Francesco Mazzeo, Egidio Di Gialleonardo, Stefano Melzi & Stefano Bruni

This is a post-peer-review, pre-copyedit version of an article published in Vehicle System Dynamics. The final authenticated version is available online at: https://doi.org/10.1080/00423114.2023.2268225

DIPARTIMENTO DI MECCANICA ■ POLITECNICO DI MILANO
via G. La Masa, 1 ■ 20156 Milano ■ EMAIL (PEC): pecmecc@cert.polimi.it
http://www.mecc.polimi.it
Rev. 0

A multibody non-linear model of the post-derailment dynamics of a railway vehicle

Matteo Santelia*, Francesco Mazzeo, Egidio Di Gialleonardo, Stefano Melzi, Stefano Bruni

Department of Mechanical Engineering, Politecnico di Milano, Via La Masa, 1 I-20156 Milan, Italy

*Corresponding author: matteo.santelia@polimi.it

Abstract

This paper presents a multibody model of the post-derailment dynamics of a railway vehicle and its impact with a derailment containment wall (DCW) built aside the line and demonstrates the use of the model in the context of the structural sizing of devices intended to mitigate derailment effects. With respect to existing multibody models of railway vehicle dynamics, the innovative features of this model are a new contact model capable to provide a plausible prediction of the derailment process despite a simple and computationally efficient formulation, and the model of the interaction between the derailed vehicle and the impacted derailment containment structure, the latter being described by a Finite Element Model. Results from the model are compared to an established multibody software for a non-derailment case, and then a comparison is performed with a measurement from a derailment experiment published in the scientific literature, finding in both cases satisfactory agreement. The model is then applied to analyse a derailment scenario caused by the sudden failure of an axle for a locomotive vehicle travelling at 300 km/h in a HS curve, deriving the peak values of the impact force and bending moment at the base of the derailment containment wall.

Keywords: derailment, post-derailment dynamics, derailment containment structure.

1 Introduction

Railways are among the safest means of transportation, yet railway accidents leading to derailment or overturing of vehicles may still occasionally occur due to different causes like improper operation, failure of the running gear, poor track condition, extreme environmental effects, impact with obstacles [1-3]. In some cases, these events may undermine the safety of passengers and of people close to the railway track. Hence, it is crucial to identify proper mitigation measures to reduce the effect of these safety-critical events.

Experiments have been carried out to artificially produce derailments and analyse their consequences, both in real tracks [4,5] and labs [6,7]. However, reproducing all the effects of a derailment in a controlled experiment appears challenging due to safety issues and high costs associated. Therefore, experimental studies mainly focus on understanding the causes of derailment, supporting the mathematical modelling of the derailment process and assessing the accuracy of derailment detector devices. The development and assessment of mitigation measures is instead mainly based on mathematical modelling and numerical simulation of the derailment process.

In particular, numerical models can describe the post-derailment dynamics of a single vehicle or the complete train set, predict the post-derailment trajectories of the different bodies involved and estimate the impact forces due to impacts among elements of the rolling stock and infrastructure. The numerical simulation of post-derailment dynamics is also a highly challenging problem, as it requires describing the motion in the large of the vehicles and their subsystems. Furthermore, large deformation may be expected for some suspension components, requiring complex mathematical models to describe their behaviour when subjected to non-standard working conditions. Finally, it is necessary to consider the possible interaction of the derailed vehicles with parts of the infrastructure that normally would not come in direct contact with the train, e.g. sleepers, ballast, fasteners. A recent review of factors influencing the post-derailment behaviour of railway vehicles, mathematical modelling, testing and derailment containment devices can be found in [8].

Mathematical modelling and simulation support the design of devices to confine the motion of the derailed vehicles, thereby reducing the risk of collision with other trains or with parts of the infrastructure surrounding the railway line. Solutions proposed in the past include the use of guidances attached to the bogie frame that engage with the gauge side of the railhead after the derailment has occurred, restraining the lateral motion of the bogie [9,10]. Alternatively, brake disks or gearboxes attached to the wheelsets may provide a similar restraint effect of lateral motion of the derailed bogies [7,9-11]. A third option is to install containment walls beside the track [13] or other infrastructure-based devices for derailment containment [14].

Brabie and Anderson first introduced the use of multibody simulation to investigate the post-derailment behaviour of railway vehicles using the software GENSYS [9,15,16]. They considered various derailment scenarios caused by failures either in the running gear or in the high rail and analysed the effectiveness of different guidance devices installed in the running gear to restrain the post-derailment motion of the vehicle. Wu and co-authors also investigated the possible use of guides, brake disks and gearboxes to restrain the motion of derailed vehicles negotiating a viaduct under the effect of an earthquake [7,11,12]. To this aim, they combined multibody simulations performed using ADAMS/Rail with the use of a dedicated software for collision detection. In all these investigations the deformation of infrastructure components impacted by the derailing vehicles was neglected. Ling et al. also considered the case of a vehicle derailing while running over a bridge, mainly focussing on the effects of derailment on the bridge structure, considering both ballasted tracks [17] and slab tracks [18]. In their work, they proposed a model of the forces produced by the interaction between the sleepers and derailed wheels. Lim and Kong studied the effect of friction between the derailed wheels and the ballast on the deceleration of the vehicles and on the final configuration of the train set at the end of the derailment [19].

Some studies can be found in the literature considering infrastructure components aimed to reduce the effect of derailments. In [20] the effectiveness of guard-rails is studied, in [21] the containment capacity and crashworthiness of a derailment containment wall (DCW) is evaluated using a finite element analysis to perform a collision simulation. Also, a limited number of experiments performed either in field or on dedicated test rigs are reported in [14,22], describing full-scale freight-bogie derailment experiments.

The use of a DCW to confine the post-derailment motion of railway vehicles running on a tangent track during an earthquake was investigated by Tanabe et al. considering a flexible model of the wall defined using the finite element model [23]. This model is restricted to the tangent track running of the train and focusses on the motion of the derailed vehicle rather than on the impact force applied to the DCW.

The paper aims to introduce a multibody model for the simulation of the post-derailment behaviour of railway vehicles running in a curve, considering all the geometric non-linearities related to the large motion of the system and the large deformation of suspension components. The paper also introduces a method to compute the impact forces exchanged by the derailed vehicle with a DCW based on the selection of suitable control points on the surface of the bogie frame and axle boxes, whose trajectory is followed during the motion of the vehicle, identifying the positions at which contact with the DCW occurs. The dynamics of the DCW during the impact with the derailed vehicle are described using a finite element model of the wall and considering in-plane frictional forces besides the normal force produced by the impact. The new model presented in the paper is designated as Post-Derailment and Impact Model (PDIM).

This model represents the first stage of a project aiming at defining the design loads for containment walls in Italian high-speed lines: the focus is on developing a computationally efficient tool that can be used to analyse a variety of derailment scenarios without requiring excessive computational effort. Hence, the main elements of novelty of the model are represented by a simplified model of wheel/rail contact enabling fast calculation of wheel/rail contact forces and yet providing satisfactory accuracy for the purposes of the study, and the method used to model the impact of the running gear with the containment wall. In future steps of the project, extensions of the model are foreseen to include the interaction of the derailed wheels with the sleepers and ballast and the interaction among vehicles in the train set through the couplers.

With respect to other published numerical methods to model the impact of a railway vehicle with a DCW, namely the one proposed by Bae and co-authors [13,21], the approach proposed in this paper does not resort to assumptions regarding the initial derailment angle and the velocity vector of the derailed car after the derailment has occurred, and instead aims at simulating the entire derailment process starting from a cause triggering the derailment which can be a failure in the running gear (as considered here) or a failure in the track or a large track geometry defect. Furthermore, whilst the modelling approach presented in [13,21] consists of a transient dynamic analysis performed on a large FE model of the train and DCW involving an order of 10^5-10^6 independent coordinates, the model proposed here involves a much lower number of independent coordinates, in the order of few hundreds, and is therefore better suited for relatively fast parametric analyses supporting the design of the DCW.

The paper is organised as follows: the multibody model of the vehicle is presented in section 2, while section 3 is devoted to the description of the wheel-rail contact model. Section 4 describes the method used to compute impact forces between the derailed vehicle and the containment wall, Section 5 presents a comparison of the results of the multibody model with results obtained from the software Simpack for a case in which the vehicle runs over the track without derailing: this comparison demonstrates the ability of the proposed model to reproduce accurately at least a standard running condition of the vehicle. Then, numerical results for a derailment scenario with a containment wall are reported. Finally, some concluding remarks are given in Section 6.

2 Vehicle model

The mathematical model considers a single vehicle with one carbody, two bogies and four wheelsets, all introduced as rigid bodies. Each rigid body is assigned six degrees of freedom (DOF), resulting in a total of 42 DOF. Primary and secondary suspensions are modelled by a set of massless non-linear lumped parameter elastic and viscous elements. Primary suspensions, connecting the bogie frames and the wheelsets, include coil springs, vertical dampers and axle-box bushings. Secondary suspensions, connecting the carbody and the bogies, include flexicoil springs, lateral dampers, yaw dampers, lateral bump-stops, anti-roll bars and traction rods. Since large relative displacements are expected to take place between the bodies in the post-derailment phase, the model also considers the bumpstops that are used for lifting the bogies and are not coming in contact during the normal operation of the vehicle.
The motion of all bodies in the model is defined with respect to an inertial reference (global reference) located at the origin of the track. The movement of each body is described using six independent coordinates, three describing the instantaneous position of the body's centre of mass (COM) and three angles describing the orientation of the body. For each body, a body-fixed local reference is also defined, having its origin at the COM of the body and axes coinciding with the principal inertia axes of the body.
Using the standard multibody formalism [24], the vectors defining the position $\boldsymbol{r}^i$ and the velocity $\dot{\boldsymbol{r}}^i$ of a point belonging to the i^{th} rigid body in the global reference are given by the following expressions:

$$\boldsymbol{r}^i = \boldsymbol{R}^i + \boldsymbol{A}^i \overline{\boldsymbol{u}}^i \tag{1}$$

$$\dot{\boldsymbol{r}}^i = \dot{\boldsymbol{R}}^i - \boldsymbol{A}^i \tilde{\overline{\boldsymbol{u}}}^i \overline{\boldsymbol{G}}^i \dot{\boldsymbol{\theta}}^i \tag{2}$$

where:

- $\boldsymbol{R}^i$ is a column vector defining the position of the body's COM in the global reference, whose scalar components are the three independent coordinates describing the position of the COM of the body;
- $\boldsymbol{\theta}^i$ is a column vector containing the three rotational coordinates of the body;
- $\boldsymbol{A}^i$ is the transformation matrix from the body's local reference to the global reference, which is function of the rotational coordinates of the body;
- $\boldsymbol{u}^i$ is the vector defining the position of the point in the local reference. This vector is constant, owing to the fact that all bodies are considered to perform a rigid motion;
- $\tilde{\overline{\boldsymbol{u}}}^i$ is a skew-symmetric matrix formed using the scalar elements of vector $\boldsymbol{u}^i$;
- $\overline{\boldsymbol{G}}^i$ is a matrix relating the time derivative of $\boldsymbol{\theta}^i$ to the components of the angular speed of the body in the body reference.

The expressions of matrices $\boldsymbol{A}^i$ and $\overline{\boldsymbol{G}}^i$ as function of the rotational coordinates of the body can be found in [24].

In symbolic form, the equations of motion describing the vehicle motion are expressed as:

$$\boldsymbol{M}(\boldsymbol{x})\ddot{\boldsymbol{x}} = \boldsymbol{Q_v}(\boldsymbol{x},\dot{\boldsymbol{x}}) + \boldsymbol{Q}(\boldsymbol{x},\dot{\boldsymbol{x}},t) \tag{3}$$

Where $\boldsymbol{x}$ is the vector collecting the 42 independent coordinates of the system, $\boldsymbol{M}(\boldsymbol{x})$ is the configuration-dependent mass matrix of the vehicle, $\boldsymbol{Q_v}$ is the vector of generalised inertia forces which are a quadratic function of the vehicle's velocity $\dot{\boldsymbol{x}}$, and finally $\boldsymbol{Q}$ is the vector of the generalized forces acting on the vehicle. This latter term can be further decomposed as:

$$\boldsymbol{Q}(\boldsymbol{x},\dot{\boldsymbol{x}},t) = \boldsymbol{Q_g} + \boldsymbol{Q_s}(\boldsymbol{x},\dot{\boldsymbol{x}}) + \boldsymbol{Q_c}(\boldsymbol{x},\dot{\boldsymbol{x}},t) + \boldsymbol{Q_i}(\boldsymbol{x},\dot{\boldsymbol{x}},t) \tag{4}$$

with $\boldsymbol{Q_g}$ is a constant vector defining the effect of weight on each body, $\boldsymbol{Q_s}$ the vector of generalised forces produced by suspension components, $\boldsymbol{Q_c}$ the vector of generalised forces arising from wheel-rail contact (or wheel-soil contact after derailment has occurred) at all wheels in the vehicle, and finally $\boldsymbol{Q_i}$ the vector describing the effect of forces generated by the impact of the vehicle with the containment wall. These equations are numerically integrated together with the equations describing the dynamics of the flexible DCW, which are introduced in Section 4.
The expressions of the mass matrix and of vectors $\boldsymbol{Q_v}$ and $\boldsymbol{Q_g}$ is derived according to standard multibody techniques. The derivation of vector $\boldsymbol{Q_s}$ for a generic suspension component is presented below, whilst the derivation of vectors $\boldsymbol{Q_c}$ and $\boldsymbol{Q_i}$ is presented in Sections 3 and 4 respectively.

2.1 Model of suspension components

Suspension components are modelled as non-linear viscoelastic elements connecting the different bodies in the vehicle. To this aim, non-linear compact force element (CMP) models of suspension components [25] are used, which include the stiffness or viscous damping properties along three directions defined in a component-specific reference system. The definition of the model of suspension components is exemplified considering a coil spring in the primary suspension.
We consider first the model of the primary coil spring: due to the expected large deformation of the spring in the derailment phase, a non-linear force-deformation relationship needs to be considered. This is done considering the scalar components of deformation and force in a spring-fixed reference with *z* axis passing through the two mount points of the spring, whilst the direction of the *x-y* axes is irrelevant, given the axial-symmetric properties of the spring in shear directions.
The vector $\boldsymbol{d}^s$ representing the scalar components of the deformation of the coil spring in the spring-fixed reference is defined as:

$$\boldsymbol{d}^s = \boldsymbol{A}^{s^T}\left(\boldsymbol{R}^i + \boldsymbol{A}^i\overline{\boldsymbol{u}}^i - \boldsymbol{R}^j - \boldsymbol{A}^j\overline{\boldsymbol{u}}^j\right) - \{l_0 \quad 0 \quad 0\}^T \tag{5}$$

where:

- Superscripts i and j denote respectively the bogie frame and the wheelset to which the coil spring is connected;
- $\boldsymbol{R}^{i,j}$ are the vectors defining the position of the COM of bodies i and j in the global reference;

- $\boldsymbol{A}^{i,j}$ are the transformation matrices from the body reference to the global reference;
- $\bar{\boldsymbol{u}}^{i,j}$ are the constant-valued vectors defining the position in the body reference of the mount points of the spring;
- $\boldsymbol{A}^{s}$ is the transformation matrix from the spring-fixed reference to the global reference;
- l_0 is the undeformed length of the spring.

The scalar components of the force generated by the spring are defined in the coil spring reference. The axial force F_z^s is defined as a function of the z component of deformation d_z^s according to the characteristic diagram shown in the lower part of Figure 1. In this diagram, k_1 is the stiffness of the spring in standard working condition. When the extension of the spring exceeds the value d_1, a steel bumpstop comes in contact restraining the further extension of the spring, producing a step change in the stiffness of the suspension, which is increased to value k_2. The steel bumpstop, shown in the left side of Figure 1, is used to keep the wheelset and bogie frame together when the bogie is lifted. Finally, when the compression of the spring exceeds d_2, the spring reaches the close-wound condition, i.e. the coils contact each other, rising the stiffness to the value k_3.

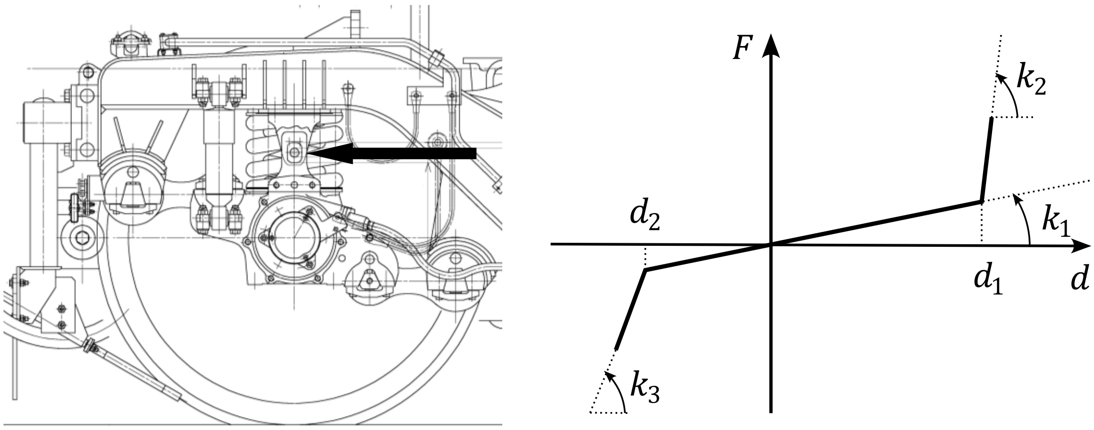

Figure 1 - Left: side view of the primary suspension (the arrow points the steel bumpstop). Right: force-deformation curve $F = F(d)$ of the suspension in vertical direction.

The two shear components of the force generated by the spring F_x^s and F_y^s are defined as proportional to the corresponding components of deformation d_x^s and d_y^s assuming through a constant shear stiffness of the spring:

$$F_x^s = k_s d_x^s \quad ; \quad F_y^s = k_s d_y^s \tag{6}$$

Finally, moments along the x and y directions of the spring reference, required to ensure the balance of the massless spring considering its length $l_0 + d_z^s$, are applied to bodies *i* and *j* [25]:

$$M_x^s = \frac{1}{2} F_y^s \left(l_0 + d_z^s\right) \quad ; \quad M_y^s = -\frac{1}{2} F_x^s \left(l_0 + d_z^s\right) \tag{7}$$

Finally, the generalised forces representing the effect of the spring on body i and body j are obtained from the principle of virtual work and are [24]:

$$\boldsymbol{Q}^i = \left\{\boldsymbol{Q}_x^{i\,T} \quad \boldsymbol{Q}_\theta^{i\,T}\right\}^T \quad ; \quad \boldsymbol{Q}^j = \left\{\boldsymbol{Q}_x^{j\,T} \quad \boldsymbol{Q}_\theta^{j\,T}\right\}^T \tag{8}$$

with:

$$\boldsymbol{Q}_x^i = -\boldsymbol{Q}_x^j = \boldsymbol{A}^s \begin{Bmatrix} F_x^s \\ F_y^s \\ F_z^s \end{Bmatrix} \tag{9}$$

$$\boldsymbol{Q}_\theta^i = \overline{\boldsymbol{G}}^{i\,T} \left(\tilde{\overline{\boldsymbol{u}}}^i \boldsymbol{A}^{i\,T} \boldsymbol{A}^S \begin{Bmatrix} F_x^s \\ F_y^s \\ F_z^s \end{Bmatrix} + \boldsymbol{A}^{i\,T} \boldsymbol{A}^S \begin{Bmatrix} M_x^s \\ M_y^s \\ 0 \end{Bmatrix} \right)$$

$$\boldsymbol{Q}_\theta^j = -\overline{\boldsymbol{G}}^{j\,T} \left(\tilde{\overline{\boldsymbol{u}}}^j \boldsymbol{A}^{j\,T} \boldsymbol{A}^S \begin{Bmatrix} F_x^s \\ F_y^s \\ F_z^s \end{Bmatrix} + \boldsymbol{A}^{j\,T} \boldsymbol{A}^S \begin{Bmatrix} M_x^s \\ M_y^s \\ 0 \end{Bmatrix} \right) \tag{10}$$

where $\overline{\boldsymbol{G}}^{i,j}$ is a square matrix of order 3 relating the components of the angular velocity of body i,j to the time derivatives of the independent coordinates describing the orientation of the body, and $\tilde{\overline{\boldsymbol{u}}}^{i,j}$ is a skew-symmetric matrix formed by the components of vector $\overline{\boldsymbol{u}}^{i,j}$, see Equation (2).

3 Wheel-rail contact model

In this work, a simplified model of wheel-rail contact is introduced, with the aim of enabling a fast, yet sufficiently accurate calculation of the contact forces. Given that the focus of the work is on modelling the post-derailment dynamics of the vehicle, the wheel-rail contact model is primarily aimed at reproducing wheel-rail contact effects during the flange climb process, particularly in terms of the vertical movement of the wheel and the ratio of the contact force components parallel and perpendicular to the top-of-rail (TOR) plane. Furthermore, the wheel/rail contact model shall represent to a sufficient degree of accuracy the contact condition for the wheels that are not subject to derailment.

For each wheel, a single contact point with the rail is assumed, and the contact forces are defined using a pre-calculated contact table which is determined from a geometric analysis. The total contact force at a given wheel-rail pair is obtained as the vector sum of a normal force and of a tangential force. The different steps of the calculation are described below.

3.1 Geometric analysis of wheel-rail contacts and interpolation of the contact table

Prior to the numerical simulation of vehicle dynamics, a geometric analysis is performed, and a contact table is defined in which all relevant geometric parameters of wheel-rail contact are stored as a function of two entry variables: the lateral shift of the wheel over the rail and the angle of attack. For each one of the two wheels in a generic wheelset, the parameters stored in the contact table are:

- Position of the contact point on the two wheels, expressed in the wheelset's body reference;
- Rolling radius variation ΔR;
- Contact angle γ;
- Wheel lift over the TOR plane h;
- Contact patch area A_0 for a nominal load N_0 = 50 kN;
- Coefficients of Kalker's linear theory C_{11}, C_{22} and C_{23};

It is assumed that all wheelsets in the vehicle have the same wheel radius, wheel profile and backflange distance, therefore the same contact table is used for all wheelsets.
At each time step, the lateral shift of the i-th wheelset Δy_w^i is obtained as:

$$\Delta y_w^i = \{0 \quad 1 \quad 0\} \boldsymbol{A}_t^{i^T} \left(\boldsymbol{R}_w^i - \boldsymbol{R}_t^i \right) \tag{11}$$

with $\boldsymbol{R}_w^i$ and $\boldsymbol{R}_t^i$ the position in the inertial reference of the origin of the i-th wheelset's body reference (coinciding with the body's COM) and of a track reference moving with the i-th wheelset and with $\boldsymbol{A}_t^i$ the transformation matrix defining the orientation of the same track reference. In a similar way, the angle of attack α_w^i of the i-th wheelset is computed. Then, the geometric parameters of wheel-rail contact at both wheels of the wheelset are obtained from the interpolation of the contact table and used to compute wheel-rail contact forces.

3.2 Normal component of wheel-rail contact force

The normal component of the contact force at each j-th wheel (j=1,2) of the i-th wheelset is defined as the vector sum of two scalar components $F_z^{i,j}$ $F_y^{i,j}$, respectively perpendicular and parallel to the TOR plane, defined as follows:

$$F_z^{i,j} = \begin{cases} k_z \left(z_w^{i,j} - h^{i,j} \right) & \text{if } z_w^{i,j} - h^{i,j} > 0 \\ 0 & \text{otherwise} \end{cases} \tag{12}$$

$$F_y^{i,j} = F_z^{i,j} tan\left(\gamma^{i,j}\right) \tag{13}$$

with $z_w^{i,j}$ the vertical position of the considered wheel in the track reference, $h^{i,j}$ the lift of the wheel obtained from the interpolation of the contact table, k_z is a stiffness parameter, chosen to be in the range of the contact stiffness defined by Hertz theory, $\gamma^{i,j}$ is the contact angle. Through the large value of the stiffness k_z, Equation (12) enforces a vertical motion of the wheel consistent to the geometry of wheel-rail contact as long as the wheel remains in contact with the rail. At the same time, Equation (13) ensures that the total force defined by the components $F_z^{i,j}$, $F_y^{i,j}$ is normal to the local contact.
The area $A^{i,j}$ of an elliptic contact patch formed by the wheel and rail is derived from the magnitude of the normal force $N^{i,j}$ and from the area A_0 under the reference load N_0 based on Hertzian contact mechanics:

$$A^{i,j} = A_0 \left(\frac{N^{i,j}}{N_0}\right)^{\frac{2}{3}} \quad \text{with} \quad N^{i,j} = \sqrt{{F_z^{i,j}}^2 + {F_y^{i,j}}^2} \tag{14}$$

and the product ab of the semi-axes of the contact ellipse are obtained as: $\frac{A^{i,j}}{\pi}$.

3.3 Tangential components of wheel-rail contact force

The procedure to compute the creep forces at the j-th wheel of the i-th wheelset is as follows. First, the position $\bar{\boldsymbol{u}}_c^{i,j}$ of the contact point in the wheelset's body reference is obtained from the contact table, as a function of the wheelset shift Δy_w^i and its angle of attack α_w^i . Using Equation (2) , the velocity vector of the contact point is obtained in the inertial reference and is projected in the wheelset's track reference and then in a wheel's contact reference $x'y'z'$ with axes pointing in longitudinal, transversal and normal direction respectively. The mathematical relationships providing the expressions for the longitudinal and transversal components of the contact point velocity $v_{x'}^{i,j}$ and $v_{y'}^{i,j}$ are omitted here for the sake of brevity but can be derived using standard multibody kinematics techniques. The component of the wheelset's angular velocity along the direction normal to contact $\omega_{z'}^i$ is also derived. From these quantities, the longitudinal, transversal and spin creepage components are derived as:

$$\begin{aligned} \xi &= \frac{v_{x'}^{i,j}}{V} && \text{longitudinal creepage} \\ \eta &= \frac{v_{y'}^{i,j}}{V} && \text{transversal creepage} \\ \phi &= \frac{\omega_{z'}^{i}}{V} && \text{spin creepage} \end{aligned} \tag{15}$$

with V the speed of the forward motion of the wheel centre.
The creep forces defined according to Kalker's linear theory are computed using the creepage components defined by Equation (15), the size of the contact patch from Equation (14) and the coefficients of the linear theory from the contact table. Then, the saturation of the creep forces is introduced according to the heuristic law by Shen, Hedrick and Elkins [26].

3.4 Generalised wheel-rail contact forces

The normal force from Equations (12)-(13) and the saturated creep forces computed as described in the previous sub-section are projected in the wheelset's body reference to form the contact force vector $\boldsymbol{F}_c^{i,j}$ and vector $\boldsymbol{Q}_c^i$ defining the generalised forces along the independent coordinates of the wheelset is computed according to the principle of virtual works [24]:

$$\boldsymbol{Q}_c^i = \sum_{j=1,2} \begin{Bmatrix} \boldsymbol{A}^i \boldsymbol{F}_c^{i,j} \\ \bar{\boldsymbol{G}}^{i^T} \tilde{\bar{\boldsymbol{u}}}^i \boldsymbol{F}_c^{i,j} \end{Bmatrix} \tag{16}$$

Finally, the generalised force vectors from all wheelsets are assembled in the single vector of generalised contact forces $\boldsymbol{Q}_c^i$ appearing in the equation of motion of the complete vehicle, see Equations (3)-(4).

3.5 Contact forces after wheel derailment

In case the lateral shift of the wheelset exceeds the minimum/maximum thresholds defined by the geometric analysis, wheel-rail contact cannot be established as the wheel falls off the track. At the present stage of development of the model, it is assumed in this case that the wheel contacts a plane parallel to the TOR. Therefore, the wheel lift $h^{i,j}$ is set to a constant value corresponding to the contact of the wheel flange with a plane located 200 mm below the TOR and a zero value is assigned to the contact angle $\gamma^{i,j}$. The normal force is then computed according to Equation (12) whilst the frictional forces are neglected. The generalised contact forces are then computed using Equation (16). It should be noted that there is no need to model the contact between the derailed wheel(s) and the side of the rails. The position of the DCW is such that either the axle-box or the bogie frame will contact the DCW before the contact between the wheel and the side face of the rail occurs.

As mentioned in the introduction, this represents a simplified model of the interaction between the wheel and the infrastructure in the post-derailment phase, and the effect of this approximation on the results presented in Section 5 should be borne in mind. However, it should be noted that the forces due to the interaction with the sleepers and ballast are mainly of dissipative nature, so the simplifying assumption made in this paper results in over-estimating the kinetic energy of the vehicle immediately before the impact, and therefore is conservative in regard of estimating the peak impact force and the peak bending moment at the base of the DCW. The extension of this model to consider the contact of the wheels with the sleepers and ballast is an ongoing development of the work.

4 Model of the impact with the derailment containment structure

This section describes the model used to estimate the impact forces caused by the contact between parts of the rolling stock and a reinforced concrete DCW built beside the track. This structure has been identified as the preferred measure to mitigate derailment effects at specific locations in the line, such as curves and viaducts, and one main goal of this research is to obtain a reliable estimation of the impact forces applied to the wall following a derailment, which can be used for the structural sizing of the wall.

The geometry of the DCW and its position relative to the track are shown in Figure 2: it is a vertical wall (i.e. parallel to the z axis of the absolute reference) whose trace in the horizontal plane replicates the geometry of the curve. The main geometric data and material properties of the DCW are provided in Table I, whilst a more detailed datasheet of the properties of the material (reinforced concrete C30/37) can be found in [27]. The height of the DCW is such that it can only come in contact with the axle boxes or with the bogie frame of the derailed bogies. The impact point is therefore close to the wall base, minimising the effect on the safety of passengers as well as the bending stresses on the DCW. Since the vehicle parts impacting the DCW are very stiff, large plastic deformations are not supposed to happen in such components. The deformation caused by the impact is expected to take place almost entirely in the DCW, mostly consisting of wall bending. It is worth noting that any deformation (either elastic or plastic) of the axle box or bogie frame occurring during the impact would result in a "softer" impact and therefore in lower peak force and bending moment caused to the wall. Therefore, the assumption of rigid behaviour for the wheelsets, axle boxes and bogie frames is conservative from the point of view of the structural sizing of the DCW.

The DCW is considered a flexible structure, using a Finite Element Model (FEM) formed by rectangular plate elements. As shown in Figure 2, the actual shape of the DCW is curved in the horizontal plane to match the geometry of the curve. However, in the FEM the curvature of the DCW is neglected because the radius of curvature (5450 m in the present work) is two-three orders of magnitude larger than the length of the region over which the impact with the vehicle takes place (approximately 10 m). Hence, a planar model is obtained. The FEM model is shown in Figure 3: it is formed by a total of 240 4-node plate elements, arranged in three rows. Each plate element is 1 m long and 0.55 m high, so the total length of the model is 80 m and the total height is 1.65 m. In-plane motion of the wall is neglected, so the only generalised nodal coordinates considered are z displacements, θ_x and θ_y rotations. Linear elastic behaviour is assumed for the material, under the assumption that the impact is not causing a major failure or permanent deformation of the wall, see also below. The equations of motion of the FEM are in the form:

$$\boldsymbol{m_w}\ddot{\boldsymbol{x}}_{\boldsymbol{w}} + \boldsymbol{c_w}\dot{\boldsymbol{x}}_{\boldsymbol{w}} + \boldsymbol{k_w}\boldsymbol{x_w} = \boldsymbol{f_w}(\boldsymbol{x}, \dot{\boldsymbol{x}}, \boldsymbol{x_w}, \dot{\boldsymbol{x}}_{\boldsymbol{w}}) \tag{17}$$

with $\boldsymbol{m_w}$, $\boldsymbol{c_w}$ and $\boldsymbol{k_w}$ the mass, damping and stiffness matrices of the FEM mdoel and $\boldsymbol{f_w}$ the vector of nodal forces corresponding to the impact forces applied to the wall by the derailed vehicle. This vector is a function of both the motion of the vehicle described by coordinates $\boldsymbol{x}$ and their derivatives $\dot{\boldsymbol{x}}$ and of the motion of the wall, described by $\boldsymbol{x_w}$, $\dot{\boldsymbol{x}}_{\boldsymbol{w}}$.

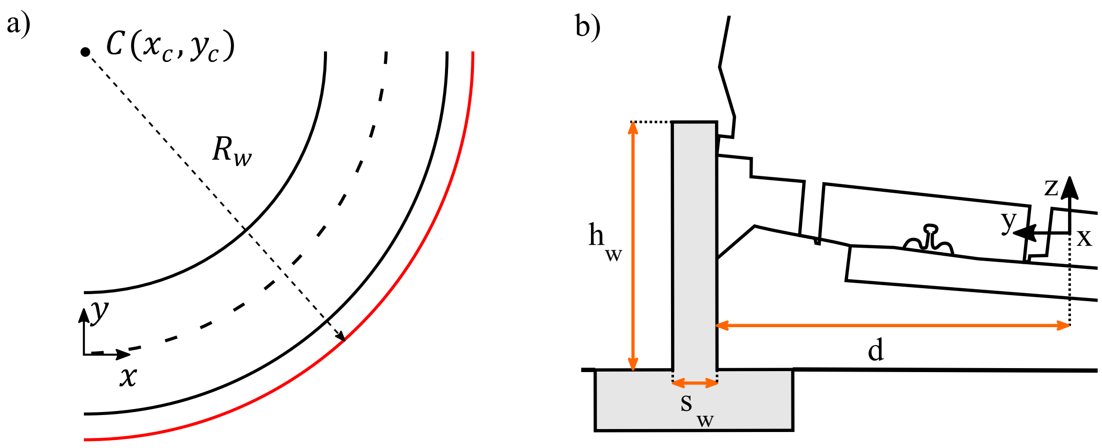

Figure 2 – a) top-view of the track (black line) and DCW (red line) b) side-view of the DCW in grey.

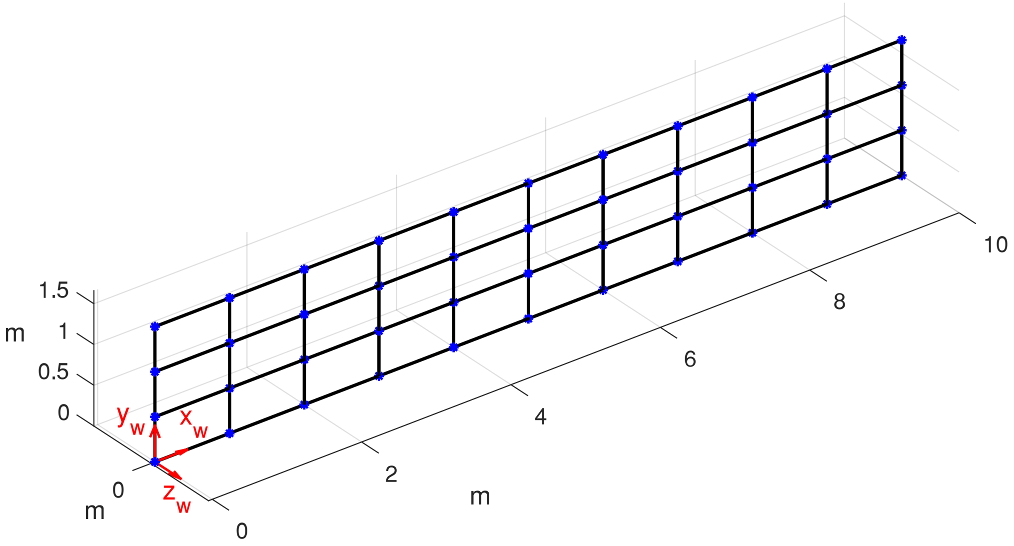

Figure 3 – Finite element model of the DCW: detail of a portion with length 10 m (the total length of the model is 80 m).

Data	Symbol	Value	Units
Geometric data			
Height	h_w	1650	mm
Thickness	s_w	300	mm
Distance form track centreline	d	2180	mm
Material data: reinforced concrete C30/37			
Density	ρ	2500	kg/m^3
Young's module	*E*	3.28E10	N/m^2
Poisson's ratio	*ν*	0.2	-

Table I - Geometrical data and material data of the derailment containment wall.

Like for the other parts of the overall MBS model, an emphasis is placed on the numerical efficiency of the procedure used to compute the impact force. With this aim, a limited number of control points is identified in the relevant bodies of the vehicle (wheelsets and bogie frames), and the trajectory of these points is evaluated during the simulation.

At each time step, a virtual compenetration δ_i between the undeformed surface of the DCW and the i-th potential contact point is computed together with its time derivative $\dot{\delta}_i$ according to:

$$\begin{gathered} \delta_i = \sqrt{(x_i - x_c)^2 + (y_i - y_c)^2} - R_w \\ \dot{\delta}_i = \dot{x}_i \frac{(x_i - x_c)}{\sqrt{(x_i - x_c)^2 + (y_i - y_c)^2}} + \dot{y}_i \frac{(y_i - y_c)}{\sqrt{(x_i - x_c)^2 + (y_i - y_c)^2}} \end{gathered} \tag{18}$$

Where:

- x_i and y_i denote the coordinates of the i-th potential contact point in the global reference system;

- $\dot{x}_i$ and $\dot{y}_i$ are the respective time derivatives;
- x_c and y_c represent the coordinates of the centre of the curve (and of the DCW);
- R_w is the radius of the DCW.

A potential contact occurrence between the vehicle and the DCW at the i-th control point is detected if $\delta_i > 0$. In this case, the component of the impact force normal to the wall $F_{N,i}$ is computed according to the Lankarani-Nikravesh model [28]. To this aim, the coordinates x_{wi} and y_{wi} of the i-th control point in the x_w-y_w-z_w reference of the DCW shown in Figure 3 are defined as:

$$\begin{aligned} x_{wi} &= V(t - t_0) + x_0 \\ y_{wi} &= (z_i - h_b) \end{aligned} \tag{19}$$

where t_0 is the first time at which a potential contact is detected, x_0 is set to 10 m and h_b is the vertical position of the base of the DCW in the absolute reference. According to Equation (19), the potential contact point is assumed to move at constant speed V across the model of the DCW, starting 10 m far from the edge: this distance is enough to neglect the effect of boundary conditions. Considering the total length of the FEM model (80 m), the location of the initial impact point allows to describe the interaction between the derailed vehicle and the impacted wall over a distance of at least 60 m, before the effect of boundary conditions becomes significant. This distance is travelled in approximately 0.7s at 300 km/h. This time interval is sufficient for the impact to occur and excite the dynamic response of the wall, as shown in Section 5.2.
From the coordinates of the potential contact point in the DCW's reference, the single k-th element in the FEM model potentially coming in contact with the vehicle at the i-th control point is found and the local coordinates ξ_i and η_i of the potential contact point in the local reference of the k-th element are easily derived. Next, the deflection of the plate element in a direction perpendicular to the DCW surface w_i and its time derivative are $\dot{w}_i$ obtained as [29]:

$$\begin{aligned} w_i &= \boldsymbol{f_k}(\xi, \eta)^T \boldsymbol{x_{wk}} \\ \dot{w}_i &= \boldsymbol{f_k}(\xi, \eta)^T \dot{\boldsymbol{x}}_{\boldsymbol{wk}} \end{aligned} \tag{20}$$

where $\boldsymbol{f_k}$ is the shape function vector of the k-th plate element evaluated at the potential contact point and $\boldsymbol{x_{wk}}$ is the vector of nodal coordinates of the k-th plate element, which is obtained as $\boldsymbol{x_{wk}} = \boldsymbol{E_k} \boldsymbol{x_w}$ with $\boldsymbol{E_k}$ a Boolean extraction matrix.
Next, the virtual compenetration of the Lankarani-Nikravesh model $\bar{\delta}_i$ and its time derivative $\dot{\bar{\delta}}_i$ are obtained as:

$$\begin{aligned} \bar{\delta}_i &= \delta_i - w_i \\ \dot{\bar{\delta}}_i &= \dot{\delta}_i - \dot{w}_i \end{aligned} \tag{21}$$

and the contact force in normal direction is computed accroding to [28] as:

$$F_{N,i} = \begin{cases} H_c\, \bar{\delta}_i^{1.5}\left[1 + \dfrac{3(1-e^2)}{4}\dfrac{\dot{\bar{\delta}}_i}{\dot{\bar{\delta}}_i(-)}\right], & \bar{\delta}_i > 0 \\ 0, & \bar{\delta}_i \le 0 \end{cases} \tag{22}$$

Where H_c is a parameter defining the Hertzian stiffness of the contact element, e is the coefficient of restitution and $\dot{\bar{\delta}}_i(-)$ is the relative approach velocity. The values of parameters H_c and e used in the simulations are stated in Section 5.3. With respect to the classic "penalty method" used in [13,21], the model of the impact force defined by Equations (18-22) allows to consider the non-linear relationship between the compenetration of the impacting bodies and the normal force, and also dissipative effects occurring during the impact.

A tangential component of the impact force is also introduced, considering a dry friction model:

$$\vec{F}_{Ti} = -\mu\, F_{Ni} \frac{\vec{V}_{Ti}}{|\vec{V}_{Ti}|} \tag{23}$$

Where μ is the friction coefficient between the vehicle and the DCW and $\vec{V}_{Ti}$ is the vector defining the component of the speed of the potential contact point tangential to the wall. However, this value is shown in Section 5.2 to have limited effect on the maximum value of the normal impact force.

The normal and frictional forces $F_{N,i}$, $F_{T,ix}$ and $F_{T,iy}$ are defined in the DCW reference. These forces are projected in the absolute reference and used to define vector $\boldsymbol{Q_i}$ in Equation (4) using standard multibody techniques.

The normal force component $F_{N,i}$ is also used to obtain vector $\boldsymbol{f_w}$ in Equation (17) representing the effect of the impact forces on the FEM of the DCW, as follows:

$$\boldsymbol{f_w} = \sum_{\boldsymbol{i}} \boldsymbol{E_k}^T \boldsymbol{f_k}(\xi,\eta) F_{N,i} \tag{24}$$

It should be noted that local damage to the DCW surface may result from the impact between the derailed vehicle and the wall. The effect of such damage on the impact forces can be considered by reducing the restitution coefficient and increasing the dry friction coefficient, as a result of increased roughness of the impacted surface. However, a sensitivity analysis performed in Section 5.3 shows that both these parameters have a limited effect on the peak bending moment at the base of the DCW, which is the main output of the model. On the other hand, assuming that the DCW is properly designed to withstand the impact against the derailed vehicle, major structural damage is not expected and therefore is not considered in the mathematical model.

5 Results

In this section, some results from the multibody model described in sections 2-4 are presented. Firstly, a 'standard' running condition is considered, where the vehicle runs through a curve from the Italian High-Speed (HS) network at the usual service speed

(300 km/h). The results for this case are compared to those obtained using a multibody model of the same vehicle defined in the software Simpack. The aim of this comparison is to show that the PDIM provides results consistent with a well-established multibody software for ordinary running conditions.
Then, the same curving condition is simulated, considering a failure in the axle of the second wheelset that leads to the derailment of the front bogie and the post-derailment dynamics is analysed until the impact with the DCW. As the Simpack wheel/rail contact module cannot natively simulate vehicle dynamics in the post-derailment phase, no comparison is possible for this case.

5.1 Comparison with Simpack in "standard" conditions

In this section the results of the PDIM are compared to those obtained from a SIMPACK model of the same vehicle. The test case considers a single ETR500 locomotive running at 300 km/h along a 5450m-radius curve with a superelevation of 120 mm. The corresponding nominal values of the non-compensated lateral acceleration in full curve is 0.49 m/s^2. The aim of this comparison is to use the SIMPACK model as a benchmark for the PDIM. Due to the fact that the SIMPACK model cannot consider the post-derailment phase, the comparison is limited to a standard running condition, not leading to the derailment of the vehicle.
Figures 4 and 5 show, as an example, the time histories of the lateral components Y (parallel to the TOR) and of the vertical components Q (parallel to the TOR) of wheel/rail contact forces for the four wheels of the front bogie, comparing the results from the PDIM and from the SIMPACK model. To allow a simpler assessment of the results, track irregularities are not considered the charts refer to the negotiation of the entry transition and the full-curve, until the vehicle settles in a steady-state. A satisfactory agreement is observed between the results of the two models, not only in terms of the steady-state values of the forces, but also during the transition. The same satisfactory comparison is obtained for other quantities relevant to vehicle dynamics and wheel/rail contact. For the sake of brevity, the time histories of these quantities are not shown, and instead the steady-state values in full curve are compared for the two models in Table II. A very good agreement between the two models is observed: the Q and Y force components of the contact force (respectively normal and parallel to the TOR) for the four wheels in the front bogies show a relative deviation which is in most cases below 1% and always below 4% and deviations in the same order are obtained for the creepages and creep force components. For the normal forces on all wheels, differences are well below 1%. The steady-state values of the creep forces $F_{l,c}$,$F_{t,c}$ (longitudinal and transversal respectively) and of the forces in the primary suspensions $F_{x,I}$, $F_{y,I}$ and $F_{z,I}$ also show relative deviations mostly in the range of 1-2% or lower and always below 5%. It can be concluded that the models of suspension components and wheel/rail contact forces introduced in sections 2 and 3 ensure a good level of accuracy at least as far as a standard running condition is considered.

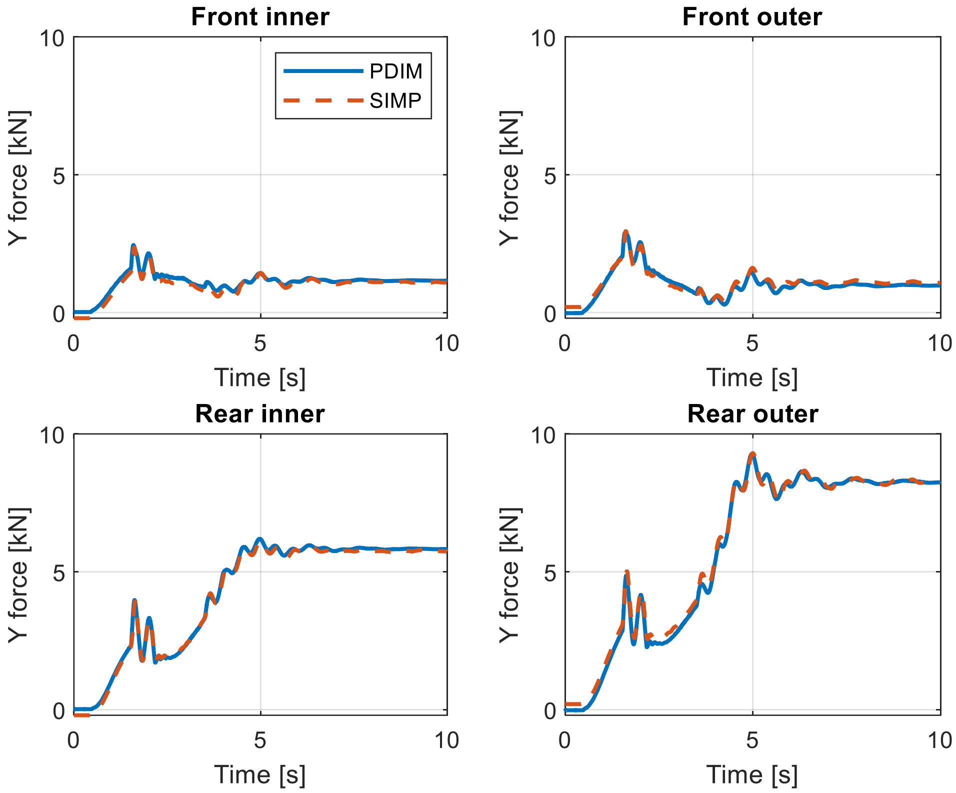

Figure 4 - Time histories of the lateral components Y of wheel/rail contact forces for the four wheels of the front bogie.

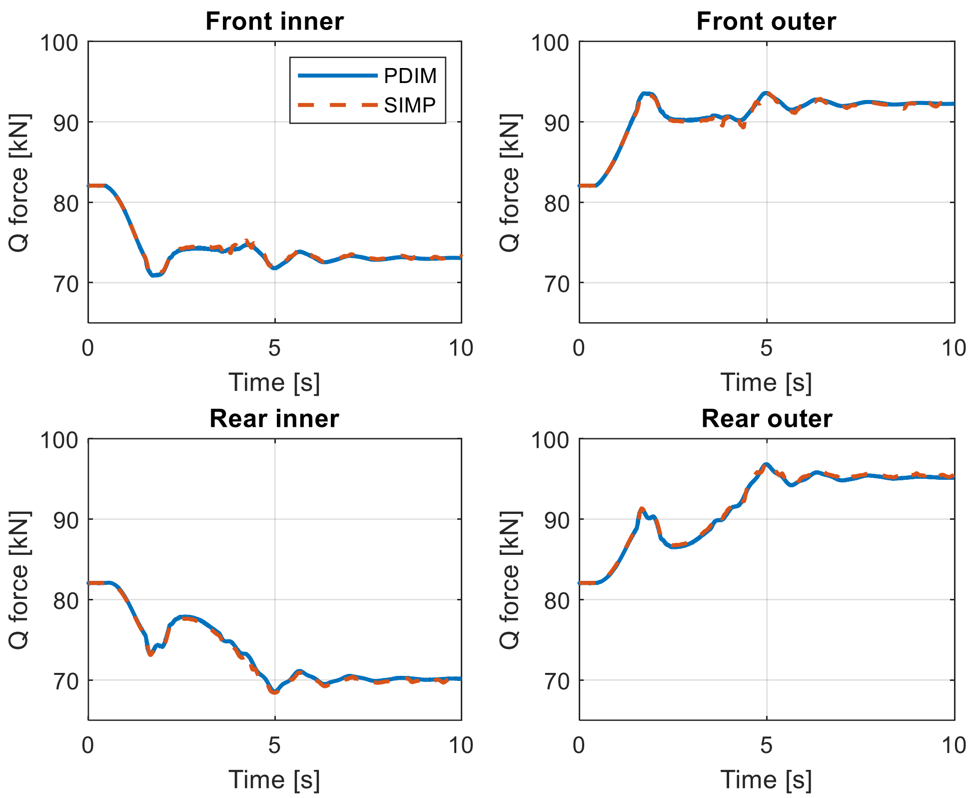

Figure 5 - Time histories of the vertical components Q of wheel/rail contact forces for the four wheels of the front bogie.

	Front inner		Front outer		Rear inner		Rear outer	
	PDIM	**SPACK**	**PDIM**	**SPACK**	**PDIM**	**SPACK**	**PDIM**	**SPACK**
$Q\ (kN)$	73.06	73.14	92.26	92.1	70.14	69.93	95.17	95.38
$Y\ (kN)$	1.06	1.1	1.09	1.1	5.73	5.75	8.35	8.25
$N\ (kN)$	73.02	73.11	92.15	92.01	70	69.8	95.47	95.68
$\xi(-)$	5.5E-04	5.4E-4	-4.0E-4	-3.9E-4	3.6E-4	3.7E-4	-2.2E-4	-2.4E-4
$\eta(-)$	-1.2E-4	-1.1E-4	-1.2E-4	-1.1E-4	-5.3E-4	-5.3E-4	-5.2E-4	-5.3E-4
$F_{l,c}\ (kN)$	-7.35	-7.23	7.34	7.22	-4.93	-4.92	4.93	4.91
$F_{t,c}\ (kN)$	2.34	2.38	-4.32	-4.12	7.29	7.13	3.37	3.42
$F_{x,I}\ (kN)$	-69.50	-69.62	-81.52	-81.39	-69.81	-69.66	-81.18	-81.33
$F_{y,I}\ (kN)$	0.82	0.86	0.95	0.99	6.79	6.77	6.91	6.89
$F_{z,I}\ (kN)$	-5.51	-5.41	5.50	5.40	-3.70	3.69	3.69	3.68

Table II – Comparison of PDIM and Simpack (abbreviated as SPACK) results: steady state values of contact forces, creepages, creep forces and forces in primary suspension.

5.2 Comparison with a derailment experiment

The results of the model were also compared to measurements from a derailment experiment published in [30]. The experiment consisted in derailing a single flatcar wagon running at approximately 50 km/h using a derailer system installed in a test track. The derailer consisted of a modification of the lateral position of one rail in the track, reducing the track gauge and forcing the opposite wheel to derail. A derailment containment provision (DCP) was installed in the centre of the track and the experiment was intended to demonstrate the ability of this device to guide the motion of the vehicle after the derailment. Reference [30] reports one single quantity measured during the experiment, which is the lateral acceleration of the wagon measured by a sensor installed on the top surface of the body frame. The measurement was low-pass filtered using a moving average with a 50 ms time window, to remove very high-frequency contents from the signal. The time history of the measured acceleration is reported in Figure 6 (top): four distinct peaks of acceleration are observed when the four axles of the wagon hit the DCP, the peak amplitude being in the range of 0.8-1.2 g.

The derailment experiment was simulated using the model described in this paper. It should be noted that in this simulation some assumptions had to be made, as the data required to define the model of the wagon are only partially available from [30]. From the photos included in the reference, it was noted that the wagon is equipped with Y25 bogies, so data for this bogie were used to create the model, while the inertial parameters of the wagon body were chosen to meet the total mass and COM height which are provided in the description of the experiment. Furthermore, no detailed information is provided in [30] about the actual geometry of the rail at the derailer system, so the lateral position of the displaced rail was assumed based on the images available in the reference.

The result of the numerical simulation is shown in Figure 6 (bottom): four peaks are clearly visible with amplitude well comparable to the ones in the measured acceleration. The simulation also reproduces a sort of ‘rebound’ (negative peak of acceleration) observed in the measurements after the second axle of each bogie hits the DCP. Considering the uncertainties inevitably related to the modelling of the derailment experiment, the agreement between the simulation result and the measurement can be considered satisfactory.

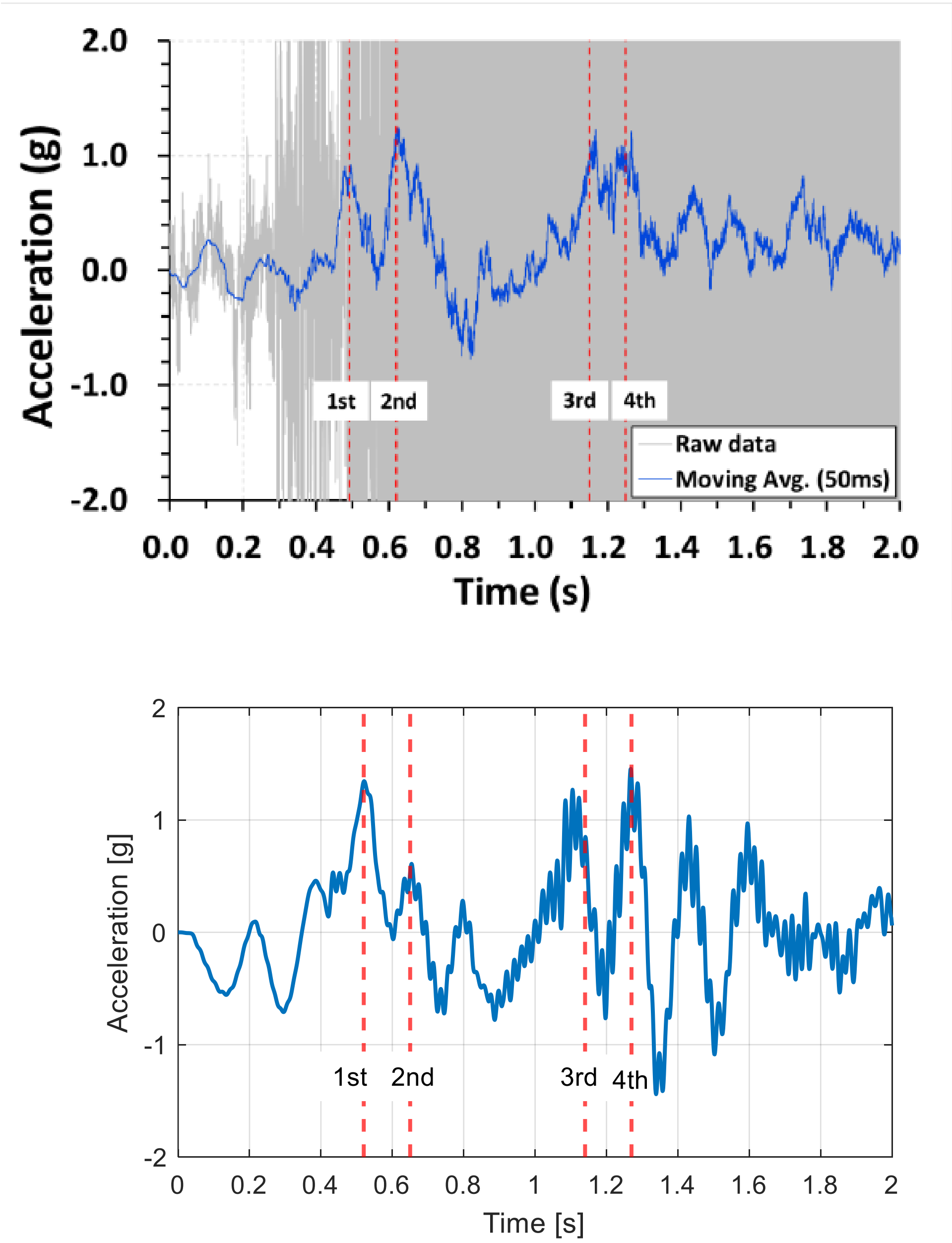

Figure 6 – Lateral acceleration of the wagon body in the derailment experiment described in [30]. Top: measured acceleration (reproduced from [30]). Bottom: result of numerical simulation.

5.3 Simulation of a derailment case and impact with the DCW

In this section, the PDIM is used to simulate a derailment condition which is caused by the failure of one collar in one of the axles of the front bogie. To consider this failure, all force components transmitted by the primary suspension to the wheelset are instantaneously set to zero, replicating the sudden loss of mechanical connection between the axle and the bogie through the primary suspension. The failure is assumed to occur on the inner side of the trailing wheelset. This is the most dangerous case because the sudden loss of vertical force at the trailing inner wheel causes a sudden decrease of the vertical force on the outer leading wheel, triggering the derailment process.

The failure is assumed to occur while the vehicle runs at 300 km/h in the constant-radius section of the curve. The dynamics of the vehicle during the derailment phase and the following motion is simulated until the front bogie impacts the DCW and the time history of the impact force is obtained. The maximum value of the impact force and bending moment at the base of the DCW can be used to define the dimensioning case for the design of the DCW. It should be noted that the ETR500 locomotive is the heaviest vehicle running on Italian HS lines and that the derailment is assumed to occur at the maximum service speed for this vehicle. Hence, the derailment condition considered maximizes the kinetic energy involved with the post-derailment motion of the vehicle, so that the impact with the DCW obtained for this derailment condition can be considered as a worst case. It should also be noted that presently the model does not consider the resistances caused by the interaction of the derailed wheelsets with the ballast and the forces exchanged by the derailed vehicle with neighbouring vehicles in the train set: these simplifying assumptions also lead to an over-estimation of the energy involved with the impact of the bogie with the DCW, so that the estimate of the maximum impact force obtained through this simulation can be considered to be conservative to some extent, compared to the real case. A more refined estimation of the impact force removing the above-mentioned simplifying assumptions is the objective of the future step of this work.
First, the phase of the simulation following immediately the failure of the axle is considered. In this phase, the derailment of the two wheelsets in the leading bogie takes place. Figure 7 shows the vertical and lateral components of the wheel/rail contact forces (blue lines) vs. the distance travelled by the vehicle after the failure of the second axle. The failure causes the sudden nulling of the vertical force transmitted by the primary suspension at the inner side of the trailing axle. As a consequence, the inner trailing wheel of the bogie loses contact with the rail and the Q force on the outer leading wheel is severely reduced (range of distance run 0-20m); at the same time, the Y force on the inner wheel of the leading wheelset increases significantly, pushing the wheelset out of the curve, due to an increase in the angle of attack of the bogie (not shown) caused by the failure in the trailing wheelset. Once this condition is established, the outer leading wheel initiates the flange climb process, which is visible from the increase of the vertical position of the contact point over the TOR z_c, also plotted in Figure 7, red line. While the flange climb process takes place, the Q and Y forces on the outer trailing wheel are subject to large fluctuations, due to impacts of the lifted inner wheel of the trailing axle with the gearbox. When the distance run by the vehicle after the failure is approximately 50 m the flange climb motion is completed and the outer wheel falls down the rail towards the field side (sudden decrease of z_c) until touching the flat plane which is used in this simulation to replace the ballast surface. In this phase, the wheel loses contact with the rail and then impacts the lower surface, then it keeps in contact with the surface while the leading wheelset, no longer restrained by the outer rail, moves away from the track centreline. Soon after the fall of the outer wheel, the inner wheel of the leading wheelset falls down the inner rail to the gauge side.
The radial motion of the COM of the two wheelsets in the front bogie is shown in Figure 8 (dotted lines). After derailing, the front wheelset (blue line) slides towards the outside of the curve, soon followed by the trailing wheelset, which is also derailed due to the axle failure. The same figure displays in solid lines the radial motion of two control points used to detect potential contacts with the DCW (see Section 4) representing the axle box of the leading and trailing wheelsets. Finally, the black solid lines in the figure show the radial position of the inner rail, outer rail and the

undeformed radial position of the DCW, while the dashed black line shows the radial position of the track centre line. The control point on the leading wheelset (blue line) contacts the DCW when the distance travelled by the vehicle after the failure is approximately 190 m, corresponding to approximately 2.3 s and afterwards mostly moves in contact with the DCW. The axle box of the second wheelset also moves radially towards the DCW and gets in contact with the wall after the vehicle has travelled a distance of approximately 240 m from the failure.

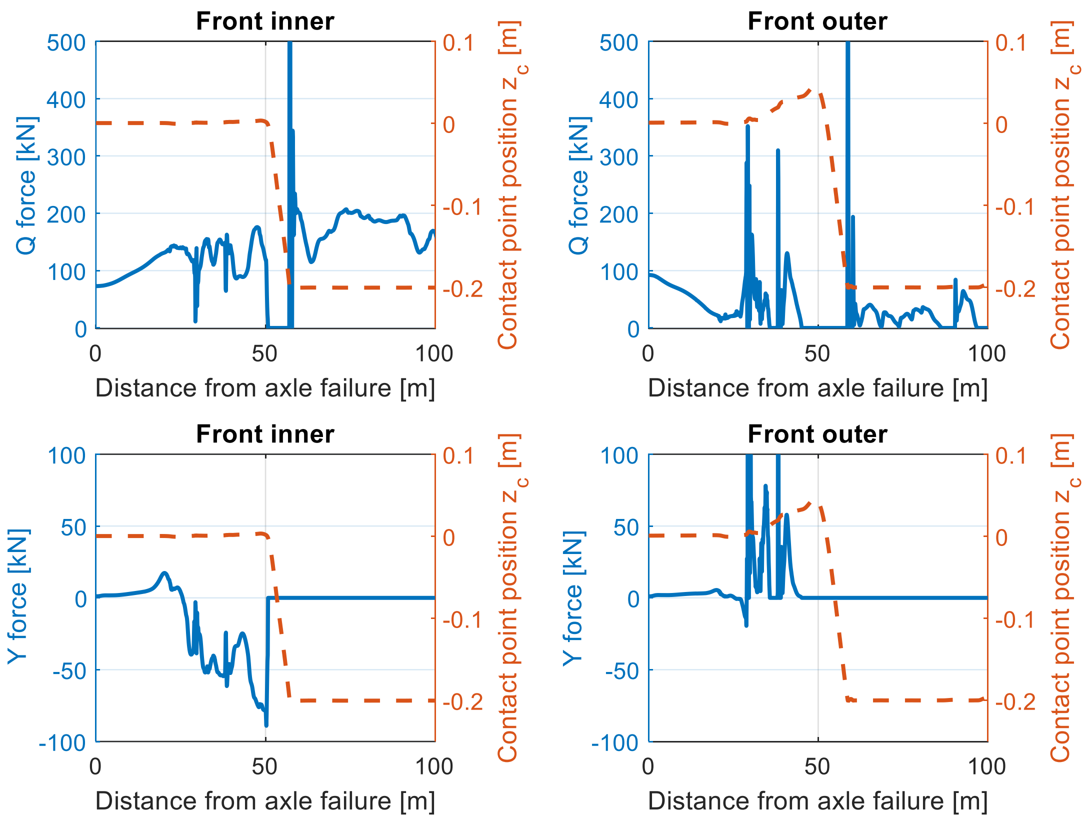

Figure 7 – Vertical (Q) and lateral components (Y) of wheel/rail contact forces and vertical position of the contact point over the TOR (z_c) for the wheels of the leading wheelset during the derailment phase, plotted vs. the distance run from the axle failure.

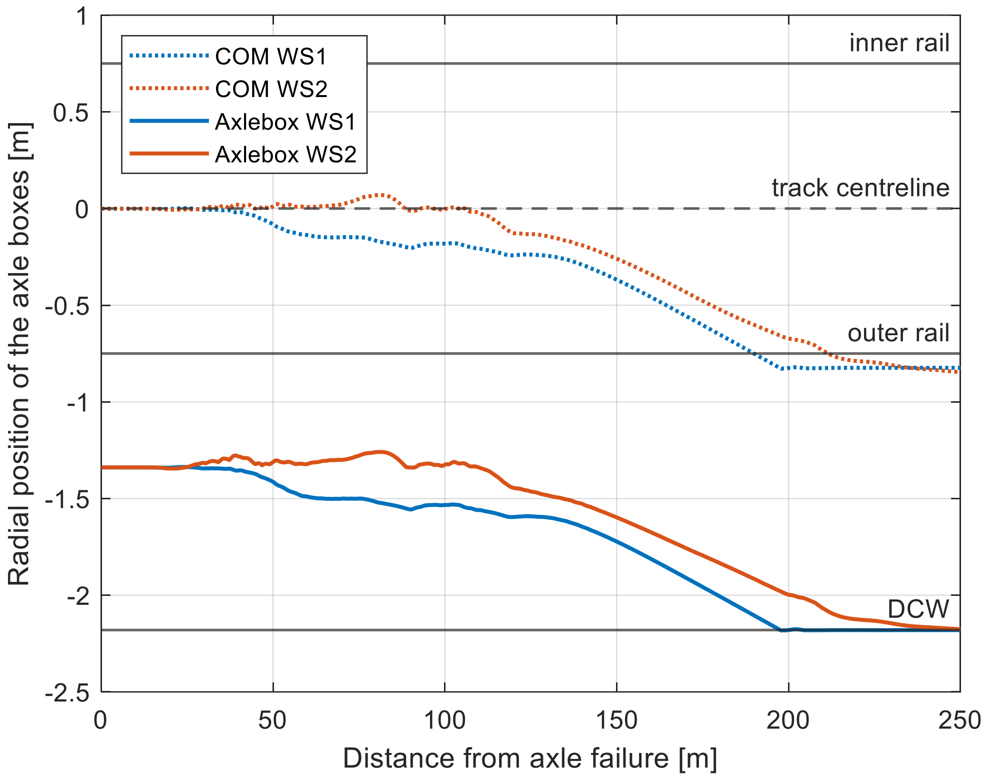

Figure 8 – Position of the centre of mass (COM, dashed lines) and of the axle boxes (solid lines) respectively of the wheelsets 1 and 2 of the front bogie.

Figure 9 shows the time history of the lateral and vertical components of the acceleration of the outer axle box in the leading wheelset. In these plots, the initial time t=0 is taken at the failure of the trailing axle causing the derailment. High peaks of acceleration are observed in both signals at some specific phases of the derailment and impact process, as shown by the labels in the figure and the related legend provided in the caption. In particular, the highest peak of lateral acceleration takes place during the impact with the DCW and reaches approximately 25 g. This value is in good qualitative agreement with the peak values of lateral axle box acceleration reported in [23], although the derailment mechanism considered in that paper is different from the one assumed here. Peaks of the vertical acceleration are observed during the derailment of both the leading and trailing wheelset, while the highest peak takes place when the outer wheel contacts the plane representing the ballast (see Section 3.5) after falling from the rail.

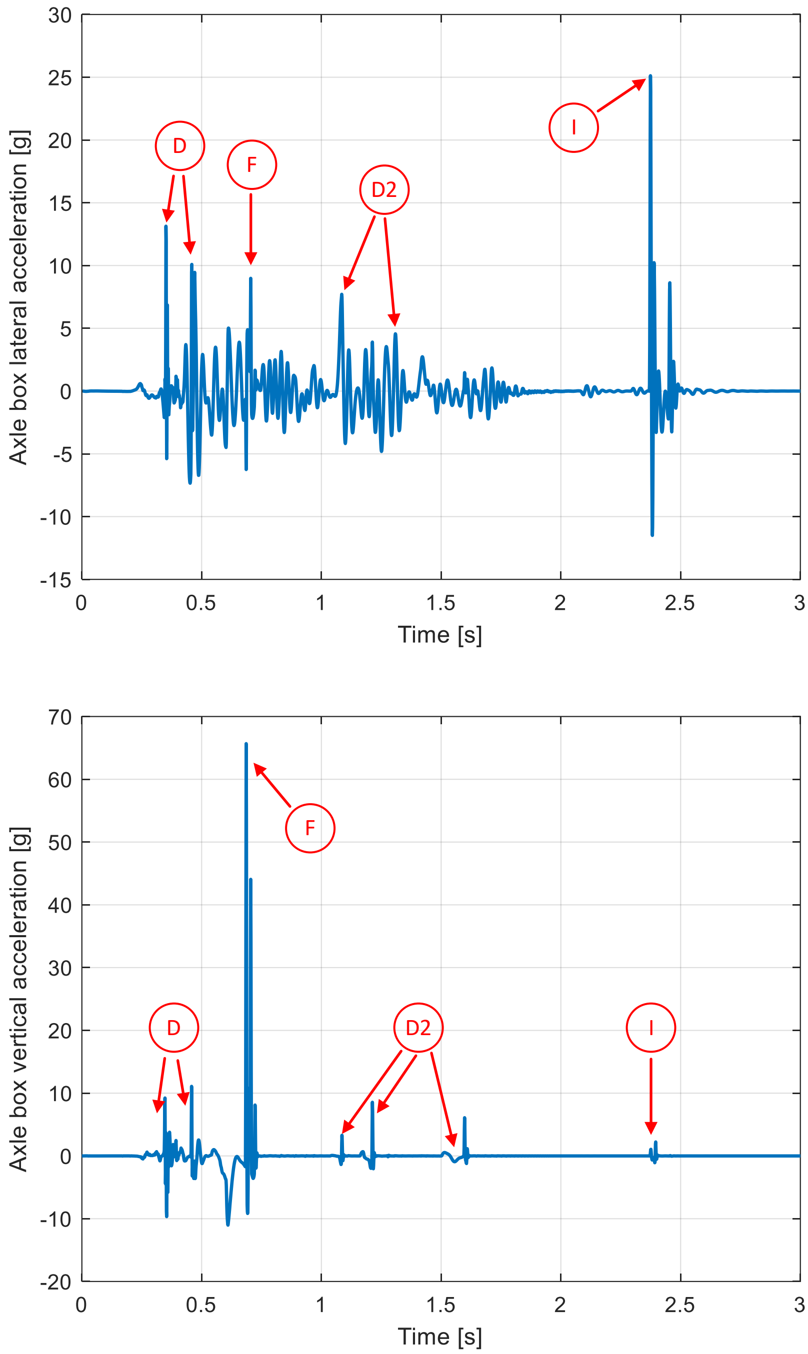

Figure 9 – Time history of the lateral acceleration (top) and vertical acceleration (bottom) of the outer axle box in the leading wheelset. Legend: D = derailment of the leading wheelset, F = the outer wheel falls on the plane representing the ballast, D2 = derailment of the trailing wheelset, I = first impact with the DCW.

Figure 10 shows the normal component of the contact force between the axle box of the leading wheelset and the DCW, plotted vs. the x_w coordinate of the contact point in the DCW reference shown in Figure 3. The blue solid line shows the results obtained with a dry friction coefficient μ equal to 0, instead for the dotted red line a coefficient μ equal to 0.6 is assume (dotted red line). Owing to the way in which the x_w coordinate is computed according to Equation (19), the first non-zero value of the impact force takes place at 10 m from the origin of the DCW reference. Focusing on the simulation with μ equal to 0, the impact force suddenly increases due to the high stiffness of the contact element considered, see Equation (22), reaching a maximum value of 435 kN. The impact force then rapidly decreases and, for a short time, the contact between the axle box and the DCW is lost. The contact is then recovered but the normal contact force remains well below the value of the initial peak. Once the oscillation of the contact force following the impact has died out, a residual force component is observed: this is due to the fact that the DCW guides the derailed bogie through a curved path having approximately the same constant radius as the full curve.

Figure 11 shows the bending moment at the base of the DCW produced by the impact, also plotted vs. the x_w coordinate of the contact point. Similarly to Figure 10, the blue solid line represents the case with a dry friction coefficient μ equal to 0; the red dotted line refers instead to a coefficient μ equal to 0.6. The value shown is the integral of the distribution of bending moments at the base of the DCW performed across the entire length of the model. Referring to the simulation with μ equal to 0, the maximum value of the bending moment takes place shortly after the initial impact and is followed by a fast oscillatory variation which is produced by the bending vibration of the DCW.

It should be noted that the results shown in Figure 10 and Figure 11 were obtained considering a value of the Hertzian stiffness parameter H_c of the contact element equal to 1.75E10 N/m$^{1.5}$. This value is just a tentative estimate, based on the Hertzian contact theory. Therefore, a sensitivity analysis was performed to investigate the effect of this parameter and the restitution coefficient e. The results are shown in Table III: increasing the stiffness coefficient H_c significantly increases the peak value of the impact force but has only a small effect on the bending moment at the base of the wall, whose maximum value decreases for increasing impact stiffness. A larger stiffness leads to a much shorter impact time and therefore to a lower impulse applied by the bogie to the wall. Based on this analysis, the value of 1.75E10 N/m$^{1.5}$ is retained in further analyses for the impact stiffness.

Table III also shows the maximum values of the impact force and bending moment for different values of the restitution coefficient e and dry friction coefficient μ, see Equations (23): both the maximum force and bending moment are weakly affected by the restitution coefficient. To explain this result, the elastic and dissipative components of the force from Eq. (22) were examined separately (not shown for the sake of brevity) and it was found that these two terms peak at different times, so that when the predominant elastic force component is at its maximum the dissipative one has already become nearly negligible, which explains the weak effect of the restitution coefficient on the peak of the total force. The increase of the dry friction coefficient μ from 0 (friction neglected) to 0.5÷0.6 has a very small effect on the peak force but increases the maximum moment by 7-10%. Dry friction modifies the dynamics of the derailed bogie after the first impact generating a yaw moment that pushes the axle box against the DCW. This is clearly visible from the zoom in Figure 10 at meter 12, where an increase of the normal force is obtained, even if its magnitude is smaller than the one immediately after the first impact. As it is visible in the zoom in Figure 11, this leads to an increase of the maximum bending moment at meter 12, that slightly overcomes the one produced after the first impact.

The computational effort required to run the simulation case presented above is 2351 s (less than 39 mins) on an Intel® Core™ i7-10750H Processor with 2.60 GHz clock. This effort refers to a simulated time of 18 s, covering the entire derailment process starting with the vehicle approaching the curve and negotiating the entry transition until reaching the full-curve section, then undergoing the derailment due to the axle failure and finally impacting the DCW. A direct comparison to other published models in terms of the computational effort required is not easy, because in most cases no data is provided in this regard. However, a comparison can be made with the model by Song et al. presented in [14]: in this paper two models, respectively defined as “real model” and “simplified model” are considered. Both models refer to a single railway bogie and the impact with a derailment containment device built inside the track gauge is considered. The total simulated time is presumably 5 s (based on the time histories shown) and the computational effort is 741 mins for the simplified model and 1545 mins for the more detailed model on a Xeon(R) E5-2687W v2 with 3.4GHz clock. Other models such as those presented in [13,21] consider a complete vehicle or train set but have a similar mathematical structure (particularly, using a FEM model of the vehicle) so it can be assumed that these models require an even higher computational effort.

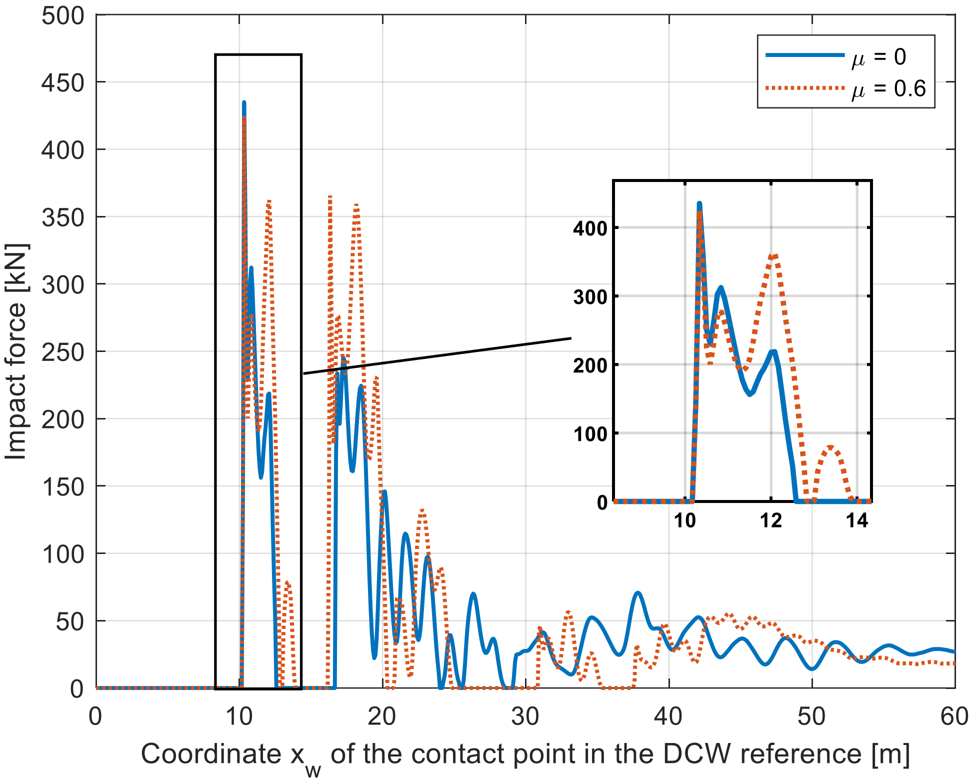

Figure 10 – Normal force on derailment containment wall of the axle box. H_c=1.75E10 N/m$^{1.5}$, e=0.5, μ=0 (solid blue line) and μ=0.6 (dotted red line).

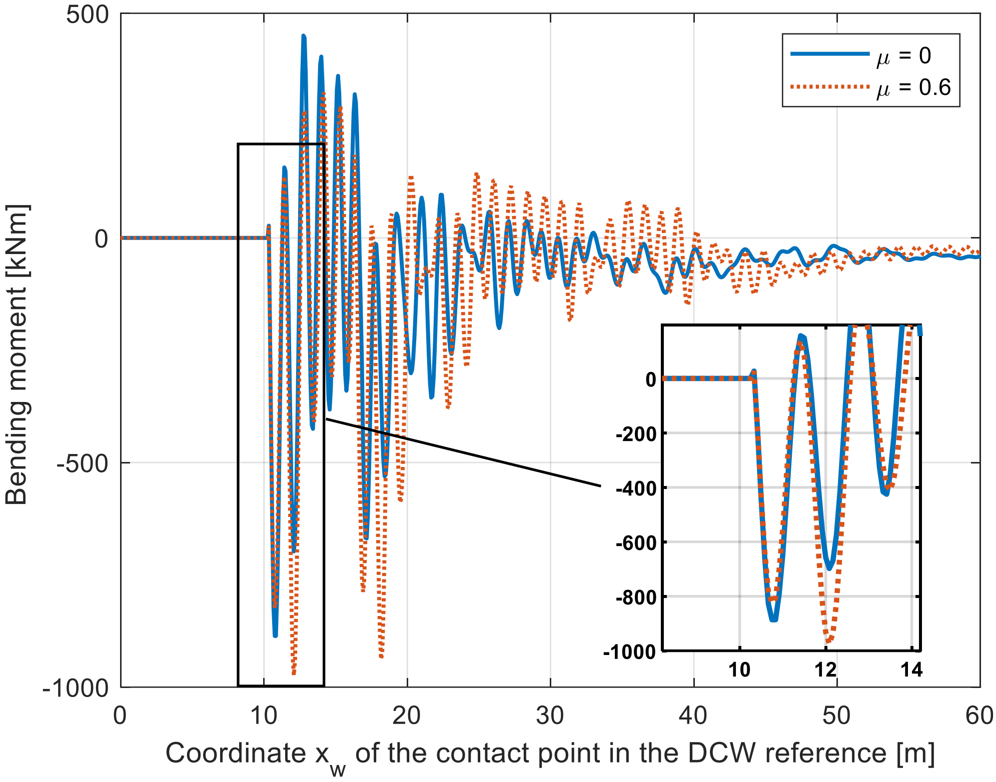

Figure 11 – Integral of the bending moment at the base of the derailment containment wall with μ=0 (solid blue line) and μ=0.6 (dotted red line). The first impact is 10 m after the starting point of the DCW.

H_c	e	μ	F	M
N/m[1.5]	-	-	*kN*	*kNm*
1.75E10	0.5	0	435	886
1.75E11	0.5	0	721	885
1.75E12	0.5	0	753	847
1.75E10	0.25	0	430	885
1.75E10	0.75	0	444	887
1.75E10	0.5	0.3	430	854
1.75E10	0.5	0.5	426	935
1.75E10	0.5	0.6	424	974

Table III – Results of the simulation in terms of maximum impact force F and maximum bending moment M: sensitivity analysis on Hertzian stiffness parameter H_c, restitution coefficient e and dry friction coefficient μ.

Finally, the mathematical model was used to perform a parametric analysis regarding the effect on the impact of train speed and distance of the DCW from the track centreline. Table IV shows the results in terms of peak impact force and bending moment for three values of train speed ranging from 300 km/h, i.e. the present service speed of the Italian HS network, to 350 km/h which is the maximum speed for which HS lines in Italy are homologated and therefore represents a prospective maximum service speed in the future. As expected, both the peak force and the peak bending moment increase with train speed, due to the higher kinetic energy involved in the derailment process. The increase of the impact force and bending moment are almost proportional to the second power of train speed, confirming that the kinetic energy of the vehicle in the post-derailment phase is the most important factor affecting the intensity of the impact.

Speed *v [km/h]*	**Peak impact force** *F [kN]*	**Peak bending moment** *M [kNm]*
300	435	886
325	505	1007
350	550	1168

Table IV– Effect of train speed on the maximum impact force and bending moment.

Table V shows the effect of the distance d of the DCW from the track centreline on the impact force and bending moment. In addition to the baseline configuration d = 2180 mm, two alternative configurations are considered with the distance $\boldsymbol{d}$ reduced to 1880 mm and increased to 2480 mm, respectively. The results show that a shorter distance of the DCW from the track results in lower impact forces and bending moments because the motion of the vehicle out of the track is contained before the derailment process is fully developed. This means that, in principle, the DCW should be located at the minimum feasible distance from the track centreline, considering the gauge assigned to the train, and other issues such as the safe disembarkment of passengers in case of emergency.

Distance from track centreline *d [mm]*	**Peak impact force** *F [kN]*	**Peak bending moment** *M [kNm]*
2180	435	886
1880	385	820
2480	528	1018

Table V– Effect of the distance of the DCW from the track centreline on the maximum impact force and bending moment.

6 Conclusions

In this paper, a multibody model of the post-derailment dynamics of a railway vehicle and impact with a derailment containment wall was presented. This model is intended to support the structural design and sizing of DCWs for the Italian HS network. The model was conceived to be computationally efficient, to enable the fast simulation of different derailment scenarios and to consider different designs of the DCW. Therefore, a simplified wheel-rail contact module is introduced which is still capable of capturing the main effects of wheel-rail contact. In the model, piecewise linear force-displacement relationships are implemented for all suspension elements to consider the effect of large deformations that may occur in the suspensions after derailment. Finally, the model incorporates a detailed description of the dynamic interaction between the derailed vehicle and the impacted DCW.

Compared to the published modelling approaches that can be traced in the literature, the model proposed here provides the following advantages:

i) a simple yet accurate model of vehicle dynamics and wheel/rail contact, enabling a fast simulation of the pre-derailment and derailment phase;
ii) an efficient algorithm to detect the interference of the derailed vehicle with the infrastructure (see Section 4), favouring the fast simulation of the post-derailment phase;
iii) the simulation of vehicle derailment is not based on assumptions such as assumed initial values for the derailment velocity vector and is instead capable of considering a realistic cause of derailment like a failure occurring in the running gear;
iv) the model considers the interaction with a flexible containment device and estimates the bending stresses produced in the containment device when impacted by the derailed vehicle; this output is key to the sizing of the derailment containment device.

The model was compared to an established multibody software (Simpack) for a non-derailment case, showing the ability of the model to capture the main effects related with vehicle dynamics in the pre-derailment phase. Furthermore, a derailment experiment published in [30] was reproduced using the model: the lateral acceleration of the derailed wagon was found to be in satisfactory agreement with the corresponding measurement published in the reference. Although this comparison cannot be regarded as a full validation of the model for the post-derailment phase, it is an encouraging first step in this direction.
The model was then applied to analyse a derailment scenario caused by the sudden failure of the second axle for a locomotive vehicle travelling at 300 km/h in a HS curve. In this condition, the model provides a plausible prediction of the derailment process and of the subsequent impact of the derailed bogie against the DCW. The computational efficiency of the model was compared to the single other model of post-derailment dynamics and impact with a DCW for which simulation times were found; a reduction of the simulation time by a factor 20 or more was found.
A parametric analysis was performed to assess the effect of some parameters of the model subject to uncertainty, namely the contact stiffness coefficient, the coefficient of restitution and the dry friction coefficient. The maximum value of the impact force is highly affected by the impact stiffness assumed in the calculation, but the bending moment at the base of the DCW is only slightly affected by this parameter and also by the restitution coefficient assumed. This is an important result, because the bending moment is the main output of the model affecting the structural sizing of the DCW, so it can be concluded that the key output of the model is weakly sensitive to a parameter (the impact stiffness) which is inevitably affected by a large uncertainty. On the other hand, the values chosen for the restitution and dry friction coefficients have a relatively limited effect on the main outputs of the model.
The effect of vehicle speed and distance of the DCW from the track centreline is also investigated and it is found that the peak impact force and bending moment at the base of the wall can be decreased to some extent by reducing the distance of the DCW from the track. As expected, the peak force and bending moment increase with vehicle speed, being approximately proportional to the square of the speed.
In the simulation of a very complex phenomenon like the post-derailment behaviour of a railway vehicle, it is unavoidable that several effects are simplified or even

neglected. The model presented here is no exception and, in particular, in its present development stage it neglects the complex interaction of the derailed wheels with the ballast and sleepers. The inclusion of these effects is targeted as the next development of the model.
The comparison of results from the presented model and measurements from derailment tests performed in full-scale is targeted soon as another development of the work presented in this paper.

References

[1] Liu X, Saat MR, Barkan CPL. Analysis of Causes of Major Train Derailment and Their Effect on Accident Rates. Transportation Research Record. 2012;2289(1):154–163.

[2] Robinson PM, Scott P, Lafaix B, et al. Development of the Future Rail Freight System to Reduce the Occurrences and Impact of Derailment- D-RAIL - Summary report and database of derailments incidents. 2011.

[3] Iwnicki S, Spiryagin M, Cole C, et al. Handbook of Railway Vehicle Dynamics, Second Edition. Boca Raton (USA): CRC Press; 2012.

[4] Diana G, Sabbioni E, Somaschini C, et al. Full-scale derailment tests on freight wagons, Vehicle System Dynamics. 2022;60(6):1849-1866.

[5] Sunami H, Morimura T, Terumichi Y, et al. Model for analysis of bogie frame motion under derailment conditions based on full-scale running tests. Multibody System Dynamics. 2012;27(3):321-349.

[6] Braghin F, Bruni S, Diana G. Experimental and numerical investigation on the derailment of a railway wheelset with solid axle, Vehicle System Dynamics. 2006;44(4):305-325.

[7] Wu X, Chi M, Gao H. The study of post-derailment dynamic behavior of railway vehicle based on running tests. Engineering Failure Analysis. 2014;44:382-399.

[8] Tang Z, Hu Y, Wang S, et al. Train post-derailment behaviours and containment methods: a review. Railway Engineering Science. 2023;

[9] Brabie D, Andersson E. On minimizing derailment risks and consequences for passenger trains at higher speeds. Proceedings of the Institution of Mechanical Engineers, Part F: Journal of Rail and Rapid Transit. 2009;223(6):543-566.

[10] Guo L, Wang K, Lin J, et al. Study of the post-derailment safety measures on low-speed derailment tests, Vehicle System Dynamics. 2016,54(7):943-962.

[11] Wu X, Chi M, Gao H, et al. Post-derailment dynamic behavior of railway vehicles travelling on a railway bridge during an earthquake. Proceedings of the Institution of Mechanical Engineers, Part F: Journal of Rail and Rapid Transit. 2016;230(2):418-439.

[12] Wu X, Chi M, Gao H. Post-derailment dynamic behaviour of a high-speed train under earthquake excitations. Engineering Failure Analysis. 2016;(64):97–110.

[13] Bae H-U, Yun K-M, Lim N-H. Containment capacity and estimation of crashworthiness of derailment containment walls against high-speed trains. Proceedings of the Institution of Mechanical Engineers, Part F: Journal of Rail and Rapid Transit. 2018;232(3):680-696.

[14] Song I-H, Kim J-W, Koo J-S, et al. Modeling and Simulation of Collision-Causing Derailment to Design the Derailment Containment Provision Using a Simplified Vehicle Model. Applied Sciences. 2020;10(1):118.

[15] Brabie D, Andersson E. Dynamic simulation of derailments and its

consequences, Vehicle System Dynamics. 2006;44(1):652-662.
[16] Brabie D, Andersson E. Post-derailment dynamic simulation of rail vehicles – methodology and applications. Vehicle System Dynamics. 2008;46(1):289–300.
[17] Ling L, Dhanasekar M, Thambiratnam DP. Dynamic response of the train–track–bridge system subjected to derailment impacts. Vehicle System Dynamics. 2017;56(4):638-657.
[18] Ling L, Dhanasekar M, Wang K, et al. Collision derailments on bridges containing ballastless slab tracks. Engineering Failure Analysis. (2019);105:869-882.
[19] Lim J, Kong J. Simplified Dynamic FEA Simulation for Post-Derailment Train-Behaviour Estimation through the Enhanced Input of Wheel–Ballast Friction Interactions. Applied Sciences. 2023;13(11):6499.
[20] Lai J, Xu J, Wang P, et al. Numerical investigation on the dynamic behaviour of derailed railway vehicles protected by guard rail, Vehicle System Dynamics. 2021;59(12):1803-1824.
[21] Bae H-U, Yun K-M, Moon J, et al. Impact Force Evaluation of the Derailment Containment Wall for High-Speed Train through a Collision Simulation. Advances in Civil Engineering. 2018;(2018):1–14.
[22] Bae H-U, Moon J, Lim S-J, et al. Full-Scale Train Derailment Testing and Analysis of Post-Derailment Behavior of Casting Bogie. Applied Sciences. 2020;10(1):59.
[23] Tanabe M, Goto K, Watanabe T, et al. A simple and efficient numerical model for dynamic interaction of high speed train and railway structure including derailment during an earthquake. Procedia Engineering. 2017;199:2729–2734.
[24] Shabana AA. Dynamics of Multibody Systems. Cambridge (UK): Cambridge University Press; 2020.
[25] Bruni S, Vinolas J, Berg M, et al. Modelling of suspension components in a rail vehicle dynamics context. Vehicle System Dynamics. 2011;49(7):1021–1072.
[26] Shen ZY, Hedrick JK, Elkins JA. A Comparison of Alternative Creep Force Models for Rail Vehicle Dynamic Analysis, Vehicle System Dynamics. 1983;12(1-3):79-83.
[27] European Committee for Standardization. EN 1992-1-1 Eurocode 2: Design of concrete structures - Part 1-1: General ruels and rules for buildings. 2005.
[28] Lankarani HM, Nikravesh PE. Continuous contact force models for impact analysis in multibody systems. Nonlinear Dyn. 1994;5:193–207.
[29] Przemieniecki JS. Theory of Matrix Structural Analysis. New York (USA): McGraw-Hill; 1968.
[30] Bae H-U, Kim K-J, Park S-Y, Han J-J, Park J-C, Lim N-H. Functionality Analysis of Derailment Containment Provisions through Full-Scale Testing—I: Collision Load and Change in the Center of Gravity. Applied Sciences. 2022; 12(21):11297.